

Variable cirrus shading during CSIP IOP 5. II: Effects on the convective boundary layer

J. H. Marsham,^{a*} A. M. Blyth,^a D. J. Parker,^a K. Beswick,^b K. A. Browning,^c U. Corsmeier,^d N. Kalthoff,^d S. Khodayar,^d C. J. Morcrette^c and E. G. Norton^b

^a University of Leeds, UK

^b University of Manchester, UK

^c University of Reading, UK

^d Universität/Forschungszentrum Karlsruhe, Germany

ABSTRACT: A combination of radiosonde, wind-profiler and aircraft observations, together with large-eddy modelling, show that shading from orphaned cirrus anvils had significant effects on the boundary layer during CSIP IOP 5. The control of boundary-layer development by the cirrus shading, and the subsidence induced by the cirrus cover, led to a boundary layer that, at an aircraft altitude of around 500 m, was less turbulent, 0.8 g kg^{-1} drier and 0.3 K warmer under thick cirrus than in clear skies. In addition, at the top of the boundary layer, turbulence persisted for some time after the onset of cirrus shading, allowing continued entrainment and so stabilization of the previously well-mixed boundary layer. These effects, which would have inhibited convective initiation under the cirrus, are consistent with the results of the first part of this study (Marsham *et al.*, 2007).

Power spectra show that, while vertical velocities were dominated by variations on the scale of the boundary-layer depth, for water-vapour mixing ratios and potential temperatures, mesoscale variations were comparable or dominant. In some cases a spectral gap is observed between these two scales of contributions. Radiosonde data and modelling show that, in addition to the variations in the boundary layer caused by the variable cirrus cover, pre-existing variations in lid strength and boundary-layer moisture were also significant on this day. These water-vapour variations are also detectable in retrievals of total-column water vapour from Global-Positioning-System data. Copyright © 2007 Royal Meteorological Society

KEY WORDS cloud shading; nonclassical mesoscale circulation; residual layer; GPS

Received 11 December 2006; Revised 9 July 2007; Accepted 25 July 2007

1. Introduction

The Convective Storm Initiation Project (CSIP) aims to improve our understanding of the processes responsible for initiating convective storms in the maritime mid-latitude climate of the UK. A total of 18 Intensive Observation Periods (IOPs) took place during a three-month period in the summer of 2005 (Browning *et al.*, 2006a). In all but one of these, the storms originated in the boundary layer (Browning *et al.*, 2006b). This contrasts with IHOP-2002, which took place in the Southern Great Plains of the USA, where approximately 50% of the storms originated from mid-levels (Wilson and Roberts, 2006). For forecasts of convective precipitation in the UK, this highlights the importance of representing the boundary layer accurately in numerical weather-prediction (NWP) models.

In the first part of this study (Marsham *et al.*, 2007), we showed that shading from orphaned cirrus anvils significantly affected convective initiation on 29 June 2005

during CSIP IOP 5. This paper discusses the observed effects of this cirrus shading on the boundary layer, from where the observed deep convection originated.

NWP models are now being used with grid spacings of approximately 1 km, which coarsely resolve convective storms but do not resolve boundary-layer convection. Sub-grid variations in thermodynamic variables are, however, assumed to lead to sub-grid variations in cloud fraction in such NWP models, unlike in most large-eddy models and many cloud-resolving models. To improve NWP models, it is essential to understand what controls boundary-layer development and variability, since even small changes in quantities such as water-vapour mixing ratio (WVMR) can control whether storms occur (Crook, 1991), and in some situations boundary-layer circulations can by themselves lead to convective initiation (Weckwerth, 1999).

The synoptic situation and convective initiation observed during CSIP on 29 June 2005 (IOP 5) were described in (Marsham *et al.*, 2007). This paper examines the effects of cirrus shading on the boundary layer. Section 2.1 discusses profile observations from radiosondes and a wind profiler, while Section 2.2

* Correspondence to: J. H. Marsham, Institute for Atmospheric Science, School of Earth and Environment, University of Leeds, Leeds, LS2 9JT, UK. E-mail: jmarsham@env.leeds.ac.uk

describes *in situ* observations from aircraft. Simulations, using version 2.3 of the Met Office large-eddy model (LEM) (Gray *et al.*, 2001), were used to interpret these observations. Section 3 uses these LEM simulations and the observations to infer the mechanisms responsible for the drier and warmer boundary layer observed at mid-levels (about 500 m) under the cirrus cover, and also discusses the role of pre-existing variations in boundary-layer moisture.

2. Observations of the boundary layer

2.1. Observed profiles

Radiosondes remain an essential tool for measuring boundary-layer thermodynamic quantities, despite the fact that they do not give sufficient spatial sampling to observe potentially-significant variability induced by boundary-layer convection (e.g. Weckwerth *et al.*, 1996). Radiosondes were launched every one or two hours from four sites (Bath, Larkhill, Chilbolton and Reading) within the area of observed convective initiation during CSIP IOP 5, each separated from its nearest neighbour by 25–50 km (Figure 1). A 1290 MHz wind profiler was also deployed at Linkenholt (20 km north of Chilbolton, Figure 1). Figure 1 shows that at 09:00 UTC Reading was covered by low stratiform cloud, while the other radiosonde sites experienced much clearer skies. By 12:00 UTC, precipitating convection had developed, while the CSIP area was under the influence of shading from orphaned cirrus anvils (Figure 1, and (Marshall *et al.*, 2007, Figure 3)).

At 08:00 UTC, all radiosondes showed a strong lid at about 500 m, capping a stably-stratified residual layer (the previous day's boundary layer), with a shallow well-mixed boundary layer close to the surface. By 10:00 UTC, surface heating had led to the well-mixed

boundary layer growing to reach this capping inversion at all radiosonde sites (Figure 2). There were already significant variations in the boundary layer at this time, before the cirrus anvils had reached any of the radiosonde sites. In particular, the lid was more pronounced at Chilbolton than at Reading, and WVMRs in the boundary layer were approximately 9.5 g kg^{-1} at Reading, 9.0 g kg^{-1} at Larkhill, 8.5 g kg^{-1} at Chilbolton and 7.5 g kg^{-1} at Bath (Figure 2). The wetter boundary layer at Reading may have been related to the dissipating low stratiform cloud observed there (Figure 1).

From 10:00 UTC onwards, the radiosonde sites were affected by cirrus shading to varying extents (Figure 2). Meteosat data show lower minimum $11 \mu\text{m}$ BTs at Chilbolton, Larkhill and Bath (around 240 K) than at Reading (around 250 K). These lowered $11 \mu\text{m}$ BTs correspond to lowered surface fluxes (Marshall *et al.*, 2007, Section 3), and both sensible and surface fluxes were linearly related to the downwelling solar irradiance (Marshall *et al.*, 2007, Figure 5). Effects of the cirrus shading on the boundary layer are clear at sites with the lower minimum $11 \mu\text{m}$ BTs (Chilbolton, Larkhill and Bath). At 12:00 UTC at Chilbolton, a stable internal layer was present (at approximately 300 m in Figure 2(a)), and this can also be seen to a lesser extent at Larkhill (at 100 m in Figure 2(c)). At these two sites at 12:00 UTC, the potential temperatures increased with height over the depths of the previously well-mixed boundary layers. In addition, at Bath the depth of the boundary layer decreased from 10:00 to 13:00 UTC, while the site was affected by cirrus cover (Figure 2(d)). None of these effects is apparent at Reading, which was less affected by cirrus cover and where the boundary layer is observed to warm more rapidly than at the other sites (Figure 2(b)).

Between 11:00 and 12:00 UTC at Reading (the radiosonde site that experienced the weakest cirrus shading), a moistening was observed between 700 m and

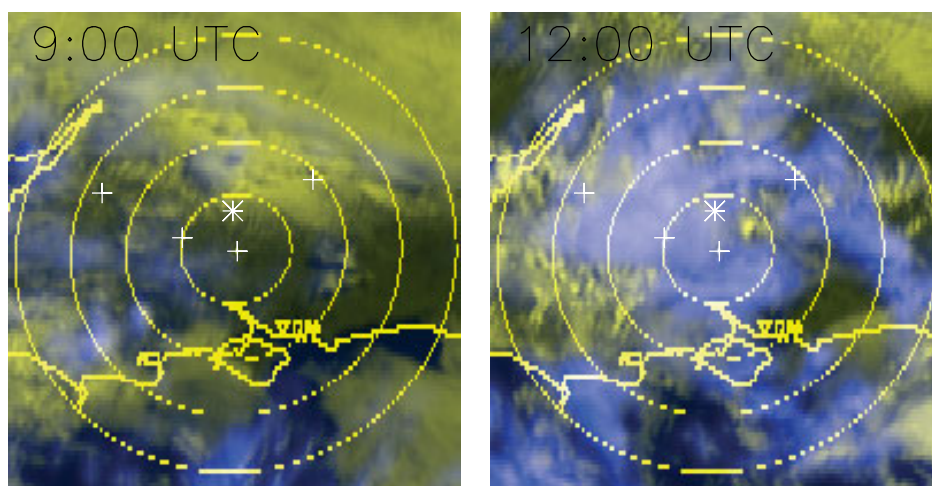


Figure 1. False-colour Meteosat images at 09:00 and 12:00 UTC. Visible top-of-atmosphere reflectance is shown in red and green, and $11 \mu\text{m}$ brightness temperature is shown in blue; hence cirrus appears blue and cumulus and stratus appear yellow and green (similar to (Marshall *et al.*, 2007, Figure 3)). Range rings are centred on the Chilbolton radar and shown at 25 km intervals. Positions of the radiosonde sites are indicated by white crosses (from west to east, these are Bath, Larkhill, Chilbolton and Reading). The position of the wind profiler at Linkenholt is indicated by the white asterisk.

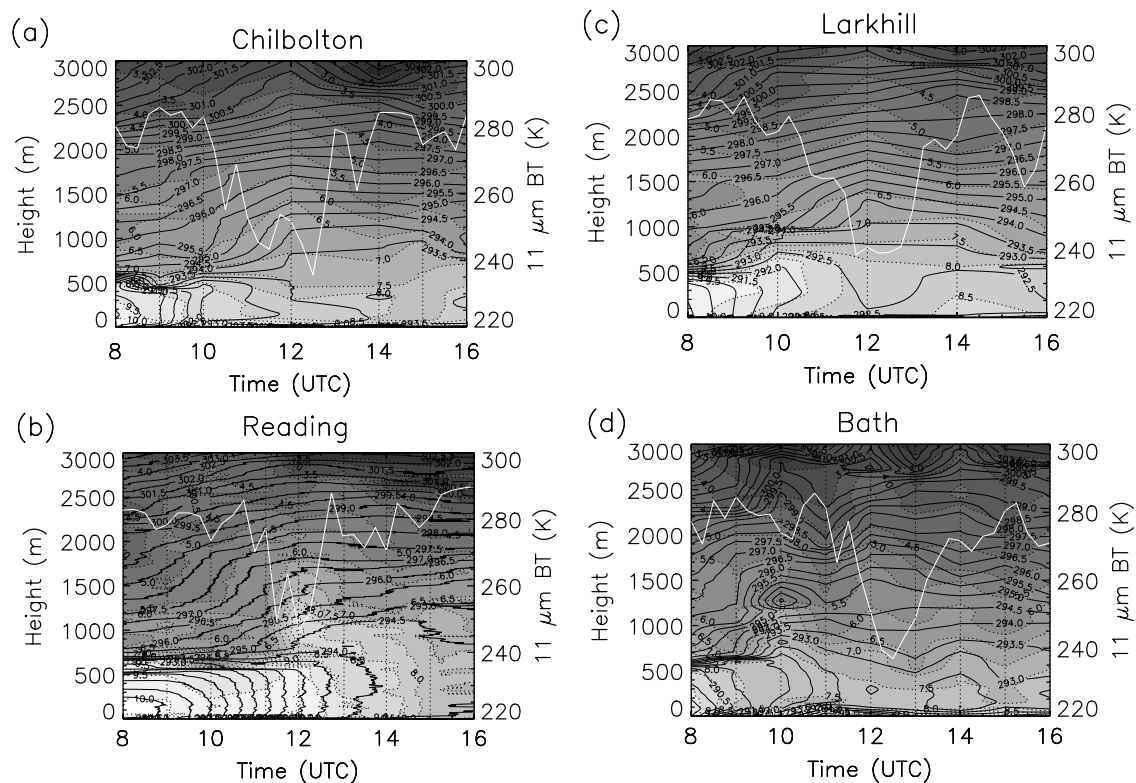


Figure 2. Time–height distributions of WVMR (g kg^{-1} , grey scale and dotted lines) and potential temperature (K, solid lines), derived from serial radiosonde ascents at (a) Chilbolton and (b) Reading. Meteosat $11 \mu\text{m}$ BTs are shown by the white lines. Radiosonde site positions are shown in Figure 1, and dotted vertical lines show radiosonde times. (c) Larkhill and (d) Bath. In (d), interpolation of data that are irregularly spaced in height has probably led to an overestimation of the depth of the super-adiabatic surface layer.

1800 m. In Figure 1, convective clouds can be seen near Reading at this time, and this moistening is presumably from convection transporting moisture out of the boundary layer and into the free troposphere. At this time Reading was at the edge of a gap in the cirrus cover, near the leading edge of the cirrus (Figure 1). A similar effect was observed at 10:00 UTC at Bath (Figure 2(d)), and again convective clouds are visible in the Meteosat data, before this site was affected by the cirrus cover. These observations of convection in gaps and in clear skies ahead of the cirrus are consistent with the conclusions of (Marshall *et al.*, 2007).

The boundary-layer profiles show continued drying after 10:00 UTC at the sites most affected by the cirrus (Bath, Larkhill and Chilbolton); this did not occur at Reading. The effects of cirrus shading on the boundary-layer moisture, and the role of the cirrus shading in this drying, are discussed in more detail in Sections 2.2 and 3.1. The variations in the boundary-layer moisture observed at the different radiosonde sites have significant effects on convective available potential energy (CAPE) and convective inhibition (CIN), and are significant for convective initiation. At 12:00 UTC, there was 640 J kg^{-1} of CAPE and 1.3 J kg^{-1} of CIN at Reading, and 150 J kg^{-1} of CAPE and 15 J kg^{-1} of CIN at Chilbolton. These values were calculated using the mean of the lowest 50 hPa, giving a mean mixing ratio of 10.0 g kg^{-1} at Reading and 8.1 g kg^{-1} at Chilbolton. If the mixing ratio from Reading were used in the

Chilbolton calculation, while keeping all other variables the same, the CAPE would increase to 840 J kg^{-1} and the CIN would decrease to 0.1 J kg^{-1} . Figure 3 shows time series of cloud-top height from two-dimensional simulations with moving positive flux anomalies (which increase surface fluxes by a factor of four and have diameters of 30 km and speeds of $10\text{--}15 \text{ ms}^{-1}$ – similar to the POS2D LEM simulations described in (Marshall *et al.*, 2007)). Clouds in the simulations using the 11:15 UTC Reading radiosonde reach their level of free convection (around 1600 m) approximately 2.5 h earlier than those in the simulations using the Chilbolton 12:00 UTC WVMR profile with the same temperature and wind profiles. This shows that the fact that the boundary layer at Reading was initially wetter and did not dry out as much as at other locations may have led to stronger storms there, rather than at Chilbolton (and the radar rain rates shown in (Marshall *et al.*, 2007, Figure 3) do perhaps suggest that the observed storms intensified near Reading).

Figure 4(a) shows data from the 1290 MHz wind profiler at Linkenholt (about 20 km north of Chilbolton, Figure 1), with the corresponding Meteosat $11 \mu\text{m}$ BTs, which show the extent of the cirrus shading (Marshall *et al.*, 2007, Section 3), superimposed. The wind-profiler signal-to-noise ratio (SNR) depends on the intensity of the radar back-scatter from refractive-index inhomogeneities on a scale of approximately half the radar wavelength (the wavelength is about 23 cm). These

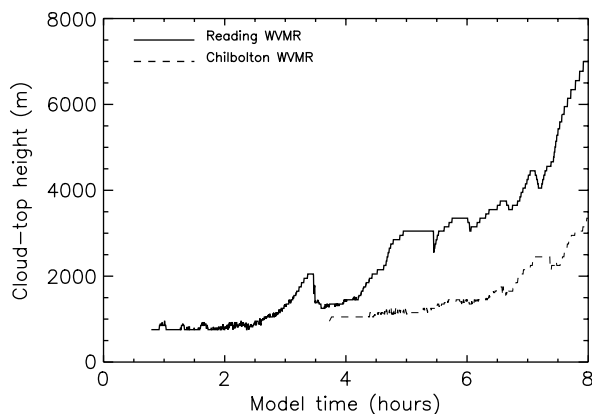


Figure 3. Time series of cloud-top heights from LEM simulations initialized using 11:15 UTC Reading radiosonde temperature and wind profiles, with different WVMR profiles. Both runs use moving positive surface-flux anomalies that increase surface fluxes by a factor of four, have diameters of 30 km, and move at 10 ms^{-1} (Marshall *et al.*, 2007, Section 4).

refractive-index inhomogeneities are therefore related not only to the mean vertical gradient in refractive index, but also to turbulent intensity. Figure 5 shows turbulent kinetic energy (TKE) from a three-dimensional LEM simulation of the boundary layer at Linkenholt. The model domain was 5 km by 5 km in the horizontal, and horizontal grid spacings of 50 m were used. Vertical grid spacings were 50 m at heights less than about 4 km. Periodic lateral boundary conditions were applied, and damping from 5500 m to the top of the model (13000 m) was used to remove gravity waves. The model was initialized with the 08:00 UTC radiosonde profile from

Chilbolton (the nearest radiosonde site to Linkenholt), and forced with surface fluxes estimated from $11 \mu\text{m}$ infrared Meteosat data from Linkenholt (Marshall *et al.*, 2007, Section 3). We expect some significant inaccuracies in such estimated fluxes (Marshall *et al.*, 2007), and the simulation neglects any change in air mass over the simulation period, but the results enable better interpretation of Figure 4, since we know that effects observed in the model are driven by the imposed surface-flux variations.

Figure 4 shows high SNRs from turbulence in the boundary layer at around 10:00 UTC, when there was little cloud cover at Linkenholt ahead of the approaching cirrus cover. The intensity of this turbulence decreased from around 11:00 UTC, and from 11:00 to 13:00 UTC the depth of the layer with SNRs above 15 dB decreased from 1400 m to 1000 m. Similar effects are seen in Figure 5; these are due to the reduction in surface fluxes at this time. The minimum in turbulent intensity, and also the depth of the turbulent boundary layer (both at around 12:45 UTC), lag the minimum surface flux by 30 min in the model (Figure 5(b)), and lag the minimum $11 \mu\text{m}$ BT by 45 min in the observations (Figure 4(b)). It can be inferred that the observed turbulence minimum at about 13:00 UTC is almost certainly due largely to the reduction in surface fluxes from the cirrus shading. The decrease in the depth of the boundary layer is smaller in the model (Figure 5) than in the observations (Figure 4). This discrepancy may be due to incorrect surface fluxes, or may be because there is no subsidence at the rear edge of the anvil in this model set-up, since the model is forced with time-varying rather than spatially-varying surface fluxes.

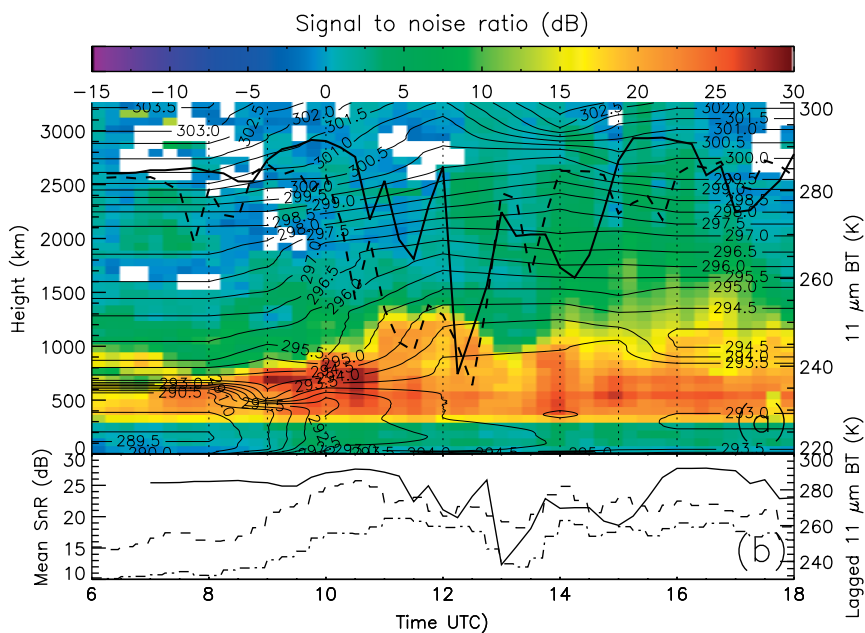


Figure 4. (a) Signal-to-noise ratio (SNR) from the 1290 MHz wind profiler at Linkenholt (about 20 km from Chilbolton) at 15 min time resolution (colour). SNR values below 300 m should be ignored. Lines show Meteosat infrared BTs for Linkenholt (thick solid line) and Chilbolton (dashed line). Contours show potential temperatures from radiosondes launched from Chilbolton. Dotted vertical lines show the radiosonde times. (b) Mean SNR from 500 m to 1000 m (dashed line, showing the turbulent intensity within the boundary layer) and from 500 m to 1500 m (dash-dotted line, more affected by the boundary-layer depth), and Meteosat infrared BTs for Linkenholt lagged by 45 min (solid line).

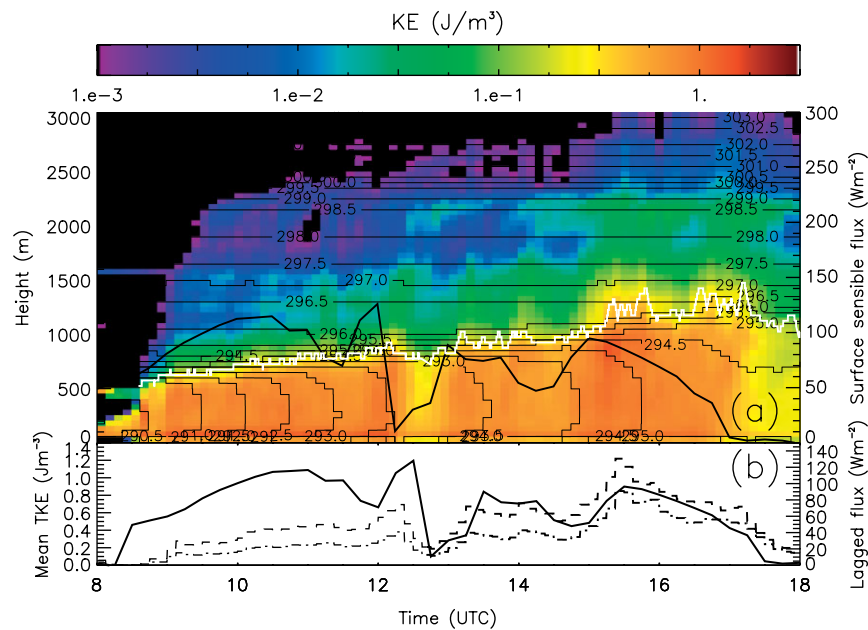


Figure 5. (a) Modelled horizontally-averaged turbulent kinetic energy (TKE) from an LEM simulation of boundary-layer development at Linkenholt (coloured), with potential temperature superimposed (contoured, solid lines). The thick black line shows the surface fluxes used, which were estimated from Meteosat 11 μm BTs. The maximum modelled cloud top is shown by the white line. (b) Mean TKE from 500 m to 1000 m (dashed line) and from 500 m to 1500 m (dash-dotted line), and the surface fluxes lagged by 30 min (solid line).

Figures 4 and 5 show that between about 12:00 and 13:00 UTC, the ‘depth of the boundary layer’ depends very much on how it is defined. Figure 5 shows that the modelled decrease in boundary-layer turbulence from 12:00 to 12:45 UTC would lead to a decrease in boundary-layer depth retrieved from the turbulence profiles, but not from potential-temperature profiles. Over this time interval, retrievals of boundary-layer depth from the SNR data, shown in Figure 4, would also show a decreasing boundary-layer depth. The boundary-layer depth defined by the potential-temperature profile from the 12:00 UTC radiosonde from Chilbolton (20 km from Linkenholt, with more cirrus shading, Figure 4) is unclear at this time, since a weak internal layer is seen below 300 m, but above this level the residual mixed layer continues to approximately 900 m.

Figure 4 shows that the observed turbulence increased again from 13:15 UTC, as cirrus cover decreased, and from 14:30 UTC significant turbulence was observed above 1500 m. The LEM results also show increased TKE above 1500 m after 15:00 UTC, although the modelled cloud top is still below 1500 m (Figure 5). Finally, higher TKEs are observed at 2300 m in LEM results (Figure 5), at the level of a thin stable layer, although the modelled cloud top had not reached these levels. This is consistent with the increased SNRs observed around 2300 m in the wind-profiler data (Figure 4). This layer is associated with sharp gradients of temperature, moisture, and hence refractive index, and these, together with the turbulence there, increase the SNR ratio. This modelled turbulence is not from modelled convection, since it is approximately 1 km above the maximum modelled cloud top (Figure 5). It is therefore inferred to be from gravity waves.

2.2. Aircraft observations of the boundary layer

Two flights took place during CSIP IOP 5: the first, by an instrumented Dornier 128, from 09:00 to 12:38 UTC towards the west of Chilbolton, and the second, by an instrumented Cessna, from 10:29 to 11:48 UTC towards the northeast of Chilbolton. Temperature, water vapour (observed using a Lyman-alpha system and a HUMICAP system), pressure, radar height above ground and radiative fluxes were measured at 1 Hz by instruments on the Dornier 128. Wind velocities were measured at 100 Hz, but values averaged to 1 Hz are used in this paper. Temperature, water vapour, pressure, radar height above ground and upwelling long-wave irradiance were measured at 1 Hz by instruments on the Cessna. The Cessna flight was at an altitude of approximately 700 m, and almost all of it was under moderate cirrus cover. When the Dornier 128 was at 420 m (before 10:41 UTC), it flew under moderate cirrus and in clear-sky regions. After 10:46 UTC, it flew at 510 m, under thick and moderate cirrus and clear skies.

A bias of $1.93 \pm 0.36 \text{ g kg}^{-1}$ was found between the Dornier 128 WVMR data and the radiosonde data. This was determined from seven comparisons between flight tracks over the Chilbolton and Bath radiosonde sites and the nearest radiosonde in time (i.e. within 33 min) over the corresponding height interval. This bias was removed for all the Dornier data presented in this paper, and the data are only used to analyse horizontal variations in moisture, rather than absolute values. The Cessna data agreed well with the radiosonde data on this day.

Figure 6 shows mean power spectra of data from all straight and level flight legs, on log-linear plots. The linear time variations of the boundary-layer variables

were removed for each leg, and the mean spectra of the level legs are plotted. Figure 6 shows $kE(k)$ plotted against k , so that the area under the curve is proportional to the variance. As a result, a peak in the curve corresponds to a significant contribution to the variance at the corresponding wave number (Jonker *et al.*, 1999). A total of 21 flight legs from the Dornier were used, with lengths between 6.9 km and 63 km. From the Cessna, 7 legs were used, with lengths between 3.3 km and 56 km. The limited number of long flight legs introduces noise to the longer-wavelength ends of the spectra.

As expected, Figure 6(a) shows that the vertical-velocity spectrum is dominated by scales of approximately 2 km, i.e. of the order of the boundary-layer

depth (Jonker *et al.*, 1999) (it is not clear whether the smaller peak at around 8 km is significant). The contributions from larger scales (greater than about 8 km) are much more significant for the WVMR and potential-temperature spectra (Figure 6(b) to (e)). This contrasts with (Mahrt, 1991), which shows more significant mesoscale variations for water vapour than for temperature. The mesoscale contributions are most pronounced for the Dornier data, where more long flight legs were available, and for these variables there is a 'spectral gap' (van der Hoven, 1957) at around 6 km separating the mesoscale contributions from a peak at a scale of approximately 2 km: the same scale as observed in the vertical-velocity spectrum (Figure 6b) and (c)). No such 'spectral gap' is observed in the power spectra from the

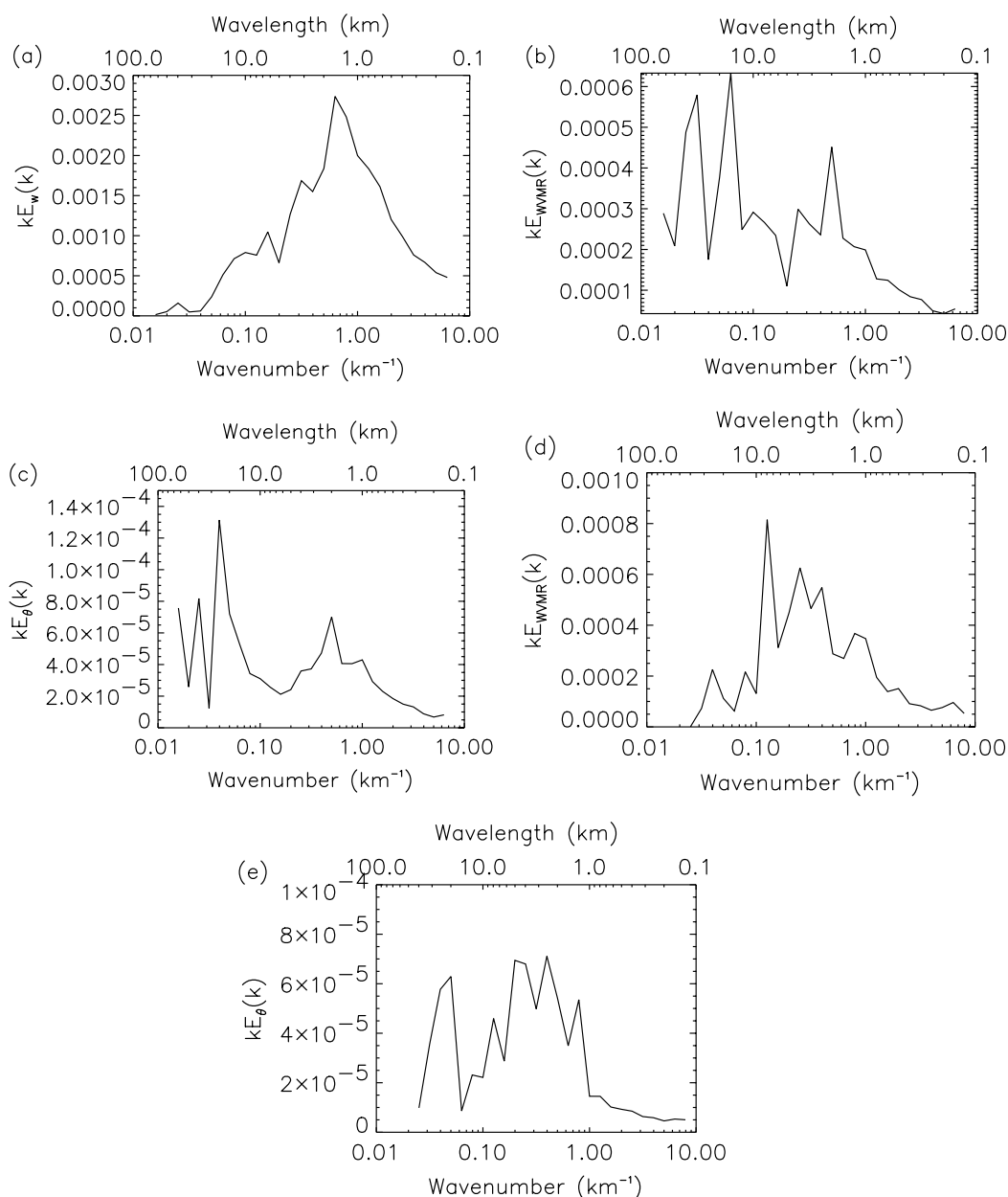


Figure 6. Power spectra of vertical wind, potential temperature and WVMR from the Dornier 128 (a, b, c); and potential temperature and WVMR from the Cessna (d, e). Log-linear plots mean that the area under a curve is proportional to the variance of the variable. (Linear time variations in the variables have been removed.)

Cessna data (Figure 6(d) and (e)). Most of the Cessna flight was under cirrus cover, and it is possible that this spectral gap is not observed for the Cessna data because the cirrus cover inhibited the boundary-layer convection, which is responsible for the peak at 2 km, and the lack of cirrus variability led to limited mesoscale boundary-layer variability.

Figure 7 shows WVMRs from the aircraft (coloured) on the corresponding 11 μm BT Meteosat images (grey scale, with darker areas showing lower BTs from cirrus cover). Figure 7 suggests that after 10:45 UTC the WVMRs observed by the aircraft in the boundary layer were related to the cirrus cover, with lower infrared BTs correlated with a drier boundary layer. This is shown more quantitatively in Figure 8. Figure 7 shows that some areas were visited twice, and the changes observed in time were related to the cirrus cover (for example, 50 km west of Chilbolton at 11:15 and 12:15 UTC). This shows that the drier boundary layer under the cirrus is not a coincidence, with the aircraft happening to have measured an already-dry region while it was under the cirrus. No relationships were found between orography and these observations of moisture in the boundary layer.

The relationships between the Dornier 128 aircraft observations and the cirrus cover are shown in Figures 8

and 9. All the correlations between boundary-layer properties observed from the Cessna aircraft and the cirrus cover were less clear, since almost the whole of the Cessna flight was affected by moderate cirrus cover; therefore the Cessna data are not shown. All the data from level Dornier flight tracks are shown, and data from before 10:41 UTC and after 10:46 UTC are shown separately to avoid changes in aircraft altitude affecting the correlations. The Meteosat data used are the closest data in space and time to each aircraft observation, with a parallax correction applied (Marshall *et al.*, 2007).

Figure 8(b) shows that the boundary layer at 510 m was drier under the cirrus cloud; this is clearest for Meteosat 11 μm BTs less than 250 K, and so is not evident when the aircraft was flying at 420 m and was under more moderate cirrus cover (Figure 8(a)). Figure 9(b) shows that at 510 m there was a correlation between Meteosat 11 μm BT and the standard deviation in the vertical wind (calculated over 50 s), which shows decreased turbulence in the boundary layer under the cirrus cover. This is consistent with the suppression of boundary-layer turbulence by cirrus shading inferred from wind-profiler data and LEM simulations (Figures 4 and 5). In addition, the data show that the standard deviations in WVMR (calculated over 50 s, or about

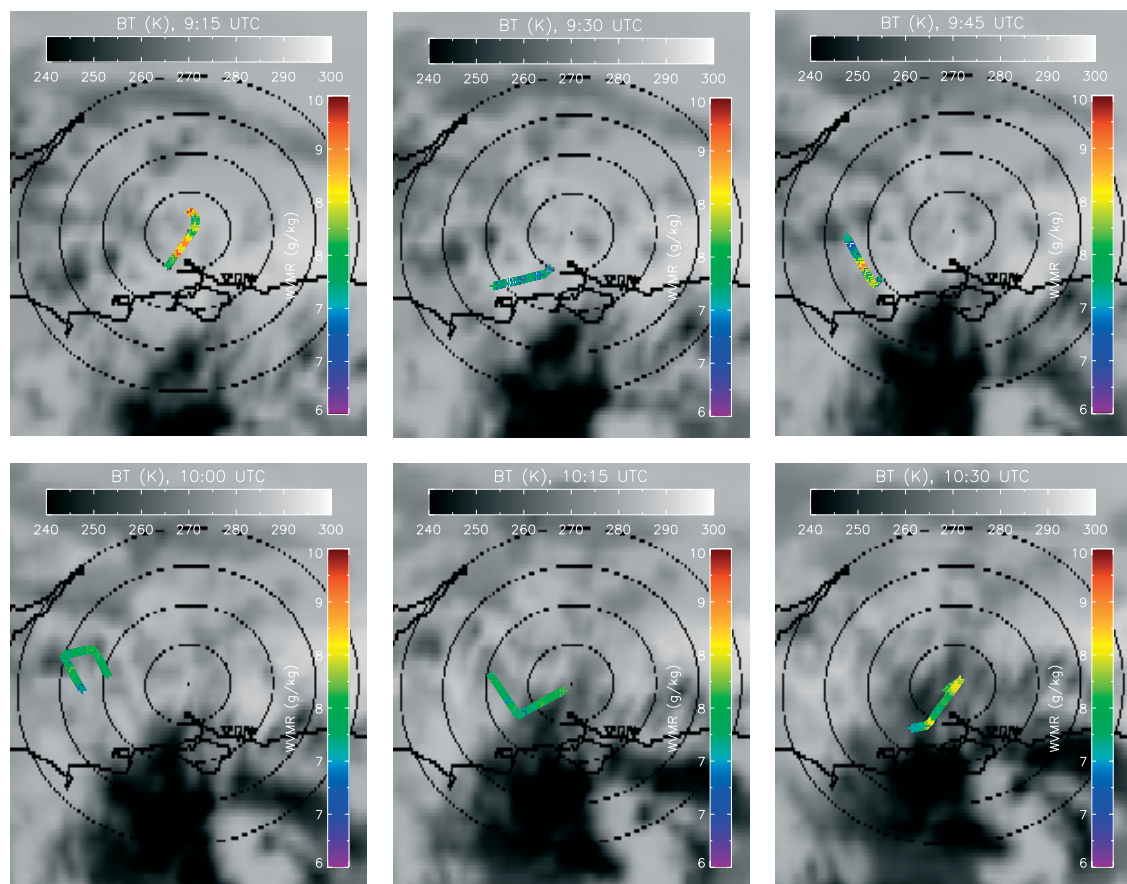


Figure 7. Meteosat 11 μm infrared BT (grey scale) and WVMR from level Dornier tracks (coloured) at 420 ± 25 m. Cirrus is shown by cold (dark) 11 μm BTs. The flight track west of Chilbolton (centre of range rings) is from the Dornier 128. Cessna data are shown north of Chilbolton.

Dornier data are from 510 ± 30 m (except those from before 10:41 UTC, which are from 420 ± 25 m). Cessna data are from 700 ± 20 m.

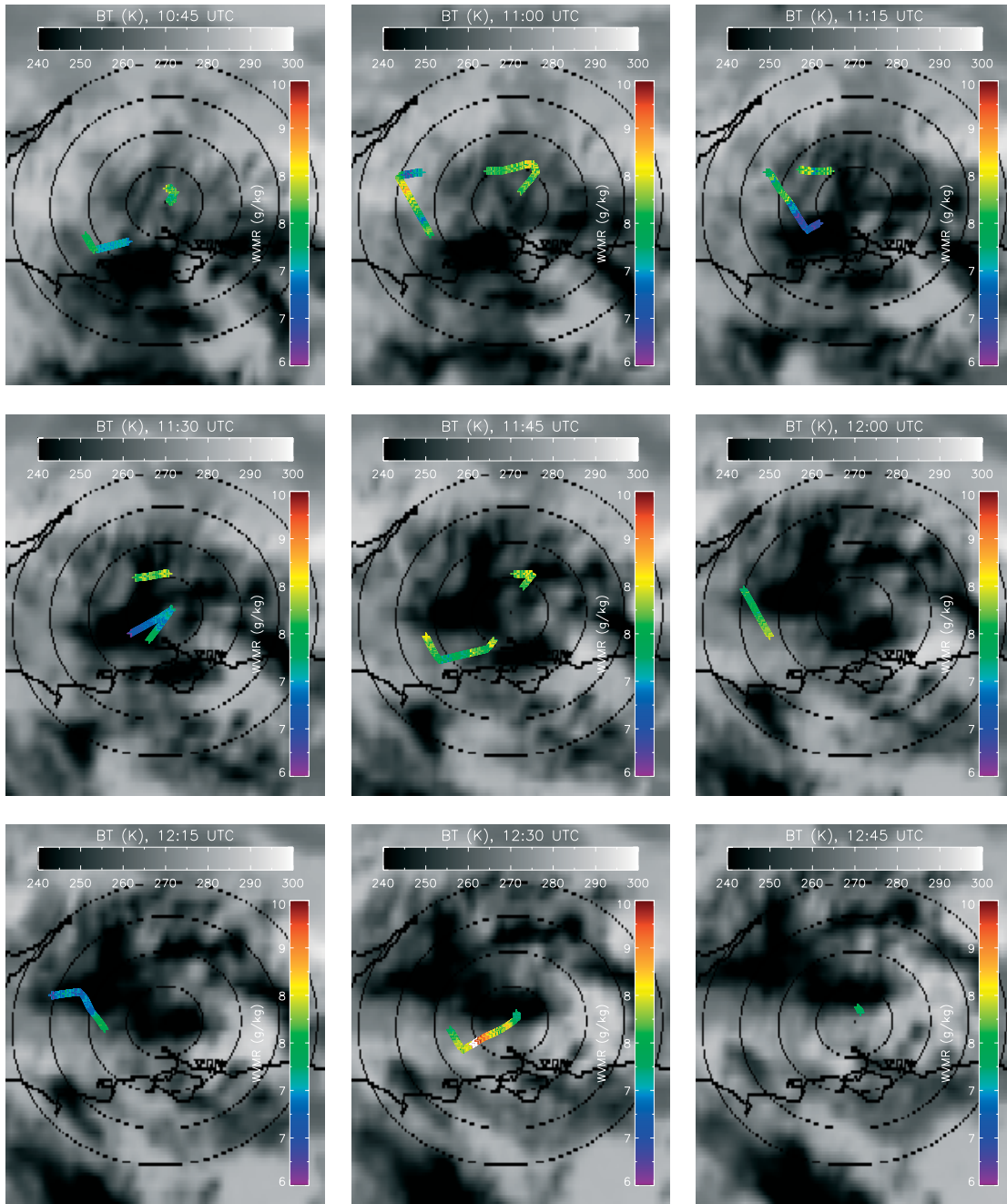


Figure 7. (Continued).

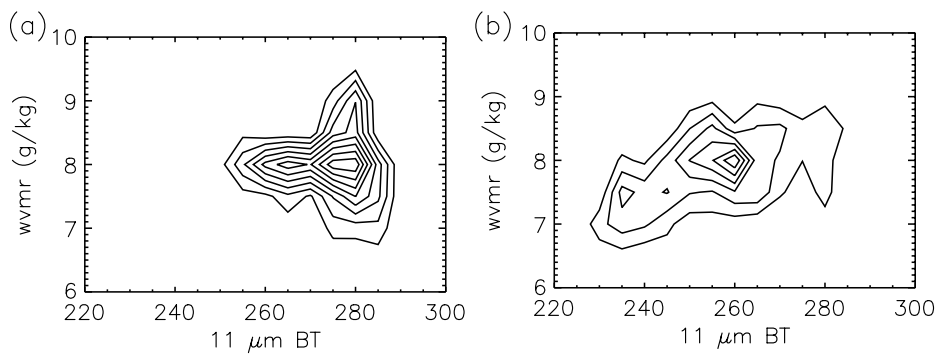


Figure 8. Bivariate probability density functions of the WVMR from the Dornier aircraft data and the corresponding Meteosat 11 μm BTs. Data are from (a) before 10:41 UTC at 420 m, and (b) after 10:46 UTC at 510 m.

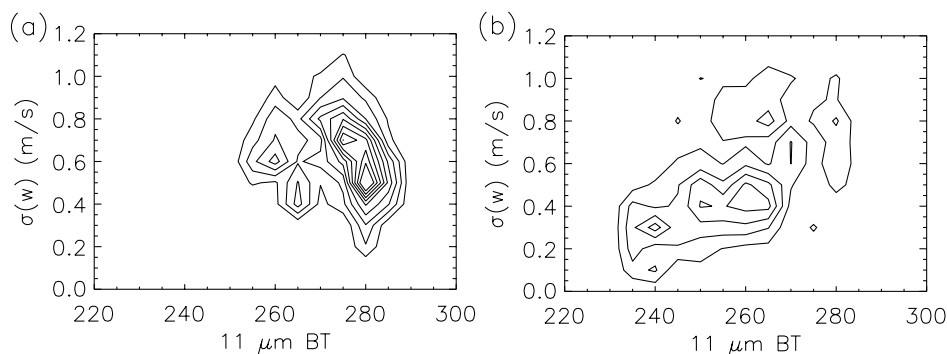


Figure 9. As Figure 8, but for the standard deviations in vertical winds ($\sigma(w)$).

3.5 km) were also larger under clearer skies, and clear skies gave lower potential temperatures in the boundary layer (not shown). There is some evidence of increased standard deviations in potential temperature in clear skies.

Figure 10 shows the correlation coefficients between aircraft observations of boundary-layer variables and Meteosat $11 \mu\text{m}$ BTs. Correlations are shown for the Meteosat data closest in time and space to the aircraft observations, and also for Meteosat data from the same locations at times before and after the aircraft observations (the Meteosat sampling time is 15 min). This shows that although the standard deviation in the vertical winds and the coincident $11 \mu\text{m}$ BTs are correlated, the correlation coefficient is higher with the Meteosat BTs from approximately 30 min earlier: i.e. the minimum in turbulence at this height lags the minimum in flux, since it takes time for the thermals to rise from the surface to the aircraft altitude of 510 m and time for the turbulence to decay (as also seen in Figures 4 and 5). Standard deviations in WVMRs correlate weakly with Meteosat data from 15 min before to 15 min after the aircraft observation time. Absolute values in WVMRs correlate best with Meteosat data 15 min after the aircraft observation time, although the correlation of Meteosat $11 \mu\text{m}$ BTs with themselves is essentially symmetric. Potential temperature has a negative correlation with the Meteosat data, and this correlation is also observed for Meteosat after the observation time.

Figure 11(a) shows that for the highest BTs (i.e. clear skies) the WVMR is correlated with the vertical wind, with moist updraughts (thermals) and dry downdraughts (due to air entrained from drier regions above the boundary layer). For the lowest BTs (thick cirrus cover) these are less correlated, and the magnitudes of the vertical winds and WVMRs are lower, as already discussed. In particular, the updraughts are weaker, and the mean WVMR is $0.82 \pm 0.01 \text{ g kg}^{-1}$ lower, for the cirrus-shaded data, not just because the updraughts here are drier, but because the downdraughts are as well.

There is no clear trend in potential temperature with vertical wind for regions with thick cirrus shading (Figure 11(b)), whereas in clear skies strong updraughts

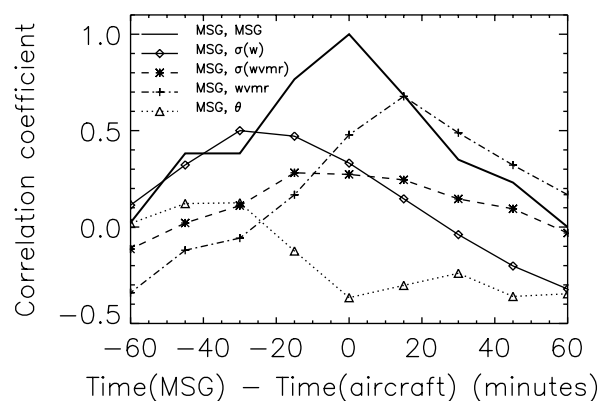


Figure 10. Lagged correlations between Meteosat $11 \mu\text{m}$ BTs and Dornier data after 10:46 UTC, as well as between Meteosat data from different times. Correlations between the Meteosat data closest to the aircraft locations from before (negative) and after (positive) the Dornier aircraft observation times are shown.

(thermals) and downdraughts (entrained air) have higher potential temperatures than regions with lower vertical winds. On average, the regions with thick cirrus shading were $0.34 \pm 0.01 \text{ K}$ warmer than the regions with clear skies. In clear skies, the variations in WVMR and potential temperature induced by the updraughts are about 0.5 g kg^{-1} and 0.2 K respectively. These variations are smaller than the mean perturbations associated with the cirrus cover (0.8 g kg^{-1} and 0.3 K), and smaller than the variability in WVMRs observed within the boundary layer before the arrival of the cirrus anvils (about 2 g kg^{-1}). This is consistent with Figure 6(b) and (c), showing that mesoscale variability dominates the variance of these variables.

The probability density functions of WVMR (Figure 12(a)) show longer tails in the distribution for the clear skies, due to active moist thermals and dry entrained air. The probability density function of potential temperature is also broader for clear skies (Figure 12(b)), and there are more strong updraughts in clear-sky regions (Figure 12(c)). Figure 12(c) also shows that there are few strong updraughts, with more numerous but weaker downdraughts. This is consistent with (Couvreur *et al.*, 2005).

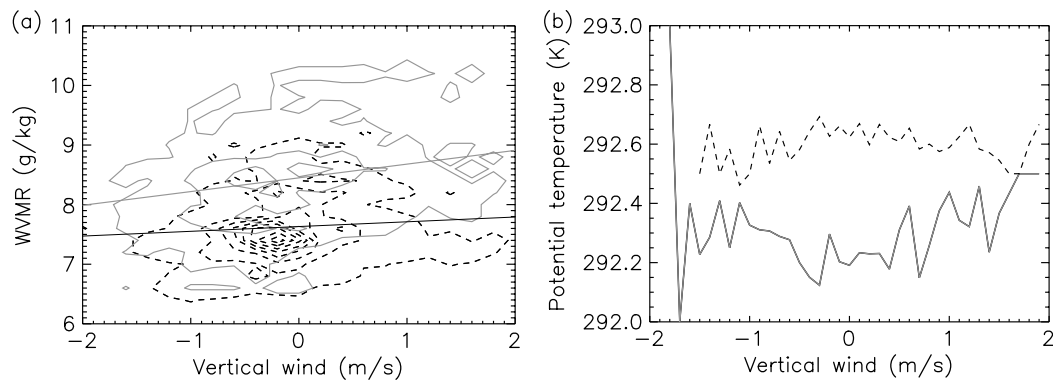


Figure 11. Boundary-layer values from level Dornier tracks at 510 m (after 10:46 UTC). Black lines show data for the coldest 25% of the corresponding Meteosat 11 μm BTs (thick cirrus); grey lines are for the warmest 25% of the Meteosat 11 μm BTs (clear skies). (a) Bivariate probability density function of vertical wind and WVMR. Straight lines show the least-squares fits. (b) Mean potential temperature as a function of vertical wind (standard errors on the means are less than 0.04 K).

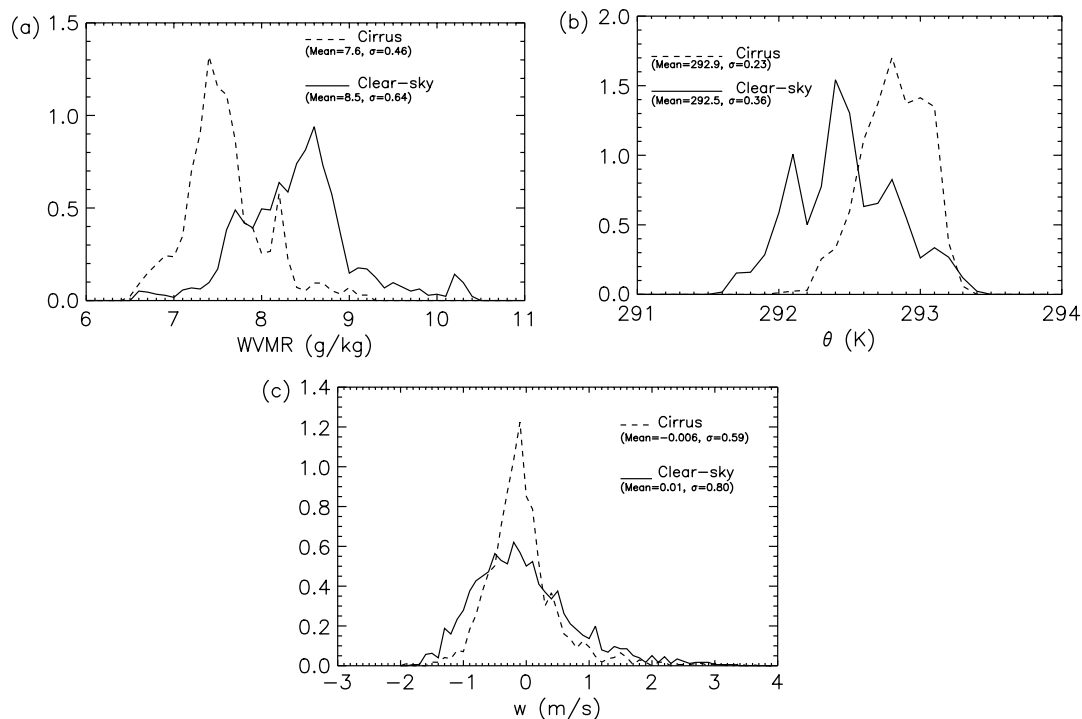


Figure 12. Univariate probability density functions of (a) WVMR, (b) potential temperature, and (c) vertical velocity, from the level Dornier tracks at 510 m (from 10:46 to 12:38 UTC). Solid lines show the densities for the warmest 25% of the Meteosat 11 μm BTs (clear skies); dashed lines show the densities for the coldest 25% of the Meteosat 11 μm BTs (cirrus).

3. Mechanisms controlling boundary-layer variables

3.1. Control of variables at mid-levels in the boundary layer by cirrus shading

The observations show correlations between boundary-layer properties and cirrus cover (Section 2.2). In particular, the boundary layer is warmer and drier under the cirrus cloud than under clear skies. The wind speeds at the cirrus altitude were much larger than within the boundary layer (15 ms^{-1} compared with 5 ms^{-1}) (Marsham *et al.*, 2007, Figure 8), so advection of any pre-existing features with the cirrus would not be expected to lead to such correlations. Instead, three effects of the cirrus

shading will be investigated. The effects on the boundary-layer heat and moisture budgets are discussed first; then the effects of the circulations induced by the cirrus; and finally the effects of shading on entrainment at the top of the boundary layer and the creation of an internal layer are examined.

Cirrus shading had a significant effect on surface fluxes, and so on boundary-layer development. Figure 13 shows results from an LEM simulation using a moving cold surface-flux anomaly (as described for NEG2D runs in (Marsham *et al.*, 2007, Table 1)). The boundary layer ahead of the cold anomaly has not yet been affected by the anomaly, so at the aircraft altitude of 500 m it is warmer and drier. The boundary layer behind the

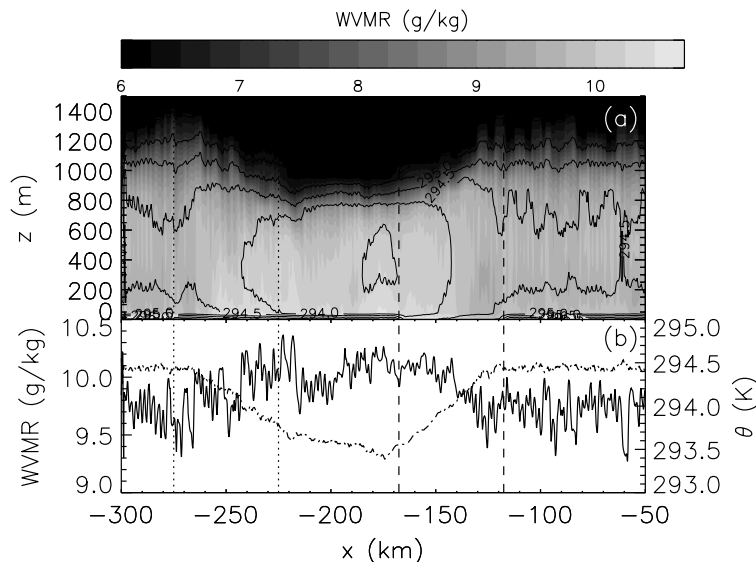


Figure 13. Results from a two-dimensional LEM simulation with a moving cold surface anomaly (reducing surface fluxes by a factor of four, with dotted and dashed vertical lines showing its initial and final positions). (a) Potential temperature (contoured) and WVMR (grey-scaled). (b) Potential temperature (dash-dotted line) and WVMR (solid line) at 500 m (approximately the altitude of aircraft flights during IOP 5). Both plots have been box-car-smoothed using a 3 km window.

anomaly has had less heat added to it, and the balance of surface fluxes and entrainment has led to a cooler, moister boundary layer here. Directly under the cirrus, the boundary layer is between these two extremes. This warmer, drier boundary layer under and ahead of the cirrus is consistent with the lagged correlations shown in Figure 10.

(Marshall *et al.*, 2007, Figure 16) shows a subsidence rate of approximately 0.01 ms^{-1} , occurring over an area approximately 50 km wide at the rear edge of the cirrus. This corresponds to a subsidence of 36 m in one hour (the anvils were moving at approximately 50 km/h). Where the aircraft flight level was near the top of the boundary layer, this could have led to a warming and drying. Radiosondes showed potential temperature increasing by approximately 0.003 K m^{-1} above the boundary layer. Therefore, 36 m corresponds to approximately 0.1 K, comparable with the observed difference of 0.3 K between the mean potential temperature observed in the boundary layer under thick cirrus and under clear skies. Furthermore, radiosonde observations from Bath (Figure 2(d)) are consistent with this process. At Bath – the radiosonde site with the thickest cirrus cover – the boundary-layer depth decreased from 11:00 to 13:00 UTC. This resulted in higher potential temperatures and lower WVMRs at 500 m at the rear edge of the cirrus (where subsidence is expected to be at its maximum, (Marshall *et al.*, 2007, Figure 16)). Wind-profiler data (Figure 4) are also consistent with a minimum in boundary-layer depth at the rear edge of the cirrus anvil.

Observations (Figures 4 and 10) show that the minimum in turbulence at 500 m lagged the maximum cirrus shading by approximately 30 min. This gives a time delay in the response of the entrainment flux to the surface fluxes. LEM simulations were used to investigate

this effect (Figure 14). The same high-resolution (50 m grid spacing) three-dimensional model set-up was used as described in Section 2, except that in this case the model was initialized with the 10:00 UTC Chilbolton radiosonde profile, and different surface fluxes were used (the relationship between surface sensible and latent heat fluxes is shown in (Marshall *et al.*, 2007, Figure 5)). High-resolution three-dimensional runs were used to ensure that entrainment processes were well resolved. The first 30 min of these simulations, which show rapidly-increasing TKE (Figure 14(b)), correspond to the model spin-up period. After 1 h of high surface fluxes, the potential temperature increases with height above approximately 600 m (Figure 14(a)), although the TKE and the time-development of the mean potential-temperature profile show that buoyant thermals (originating from the super-adiabatic surface layer) are causing mixing up to at least 800 m (Figure 14(b)). When, after 1 h, the surface fluxes have decreased to a small but positive value, a stable internal layer forms. Entrainment continues at the top of the boundary layer (at about 600 m), increasing the potential temperatures there (Figure 14(c)). This results in the potential temperature increasing with height within the boundary layer (seen at 1.25 h in Figure 14(a), (b) and (c)). Such stable internal layers are also seen within the boundary layer at Larkhill and Chilbolton at 12:00 UTC, when cirrus cover was maximum (Figure 2(a) and (c)). When surface heat fluxes are increased after 1.5 h, the warm moist thermals take some time to break through the stratification (Figure 14(c)). However, Figure 14(d) shows that if the surface fluxes are not reduced after 1 h (corresponding to no cirrus shading), one obtains a warmer, drier boundary layer under clear skies than under the cirrus cover. Therefore, the LEM simulations show that this trapping of moist thermals and entrainment

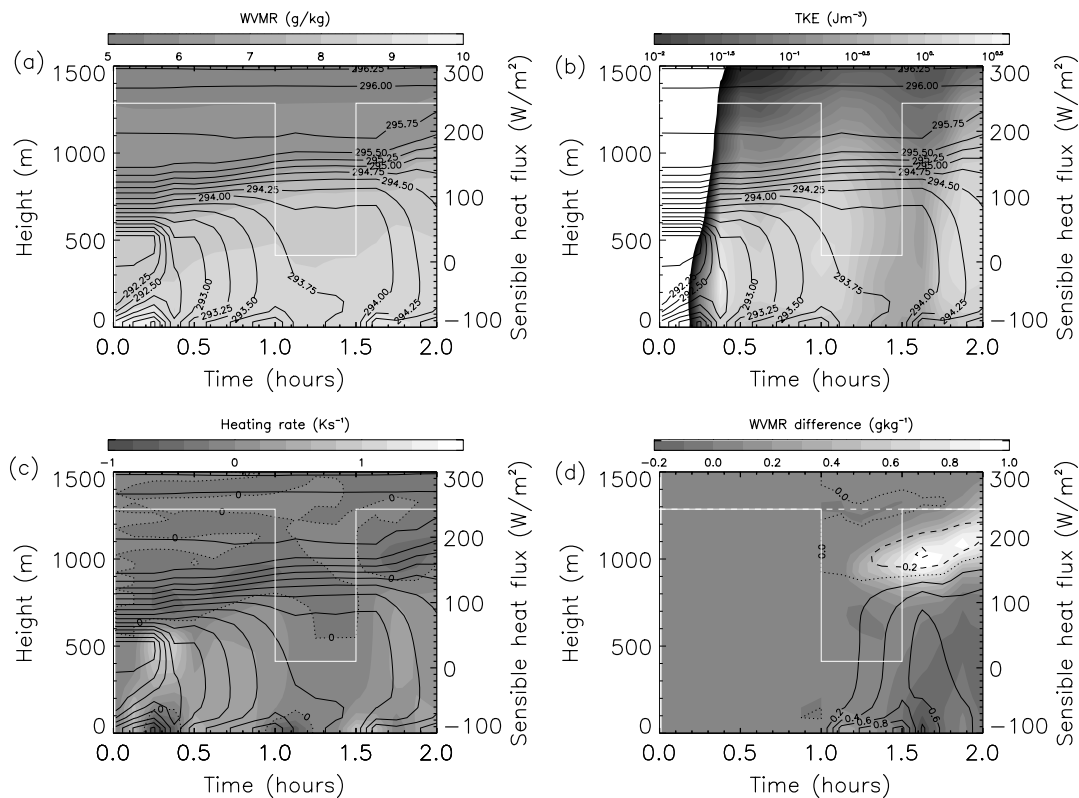


Figure 14. (a, b, c) Time series of potential-temperature profiles (solid lines), and grey-scaled (a) mean profiles of WVMR, (b) TKE profiles, and (c) heating rate (dotted line shows zero contour), for LEM simulations initialized with the 10:00 UTC Chilbolton radiosonde profile. Surface-sensible-heat fluxes (white lines) are decreased for 30 min after 1 h of simulation. The latent-heat flux increases linearly with the sensible-heat flux, but is positive for a zero sensible flux (Marsham *et al.*, 2007). (d) Potential temperature (contoured) and WVMR (grey-scaled, dotted line shows zero contour) differences between a run where the heat fluxes were not decreased after 1 h (dashed white line) and the standard run (with heat fluxes decreased after 1 h, solid white line).

drying of the boundary layer is not expected to have led to the warmer, drier boundary layer under the cirrus cloud.

In summary, two mechanisms led to the observed drying under the cirrus. Firstly, cirrus shading led to a boundary layer that was cooler and moister behind the cirrus than ahead of and under the cirrus cover (Figures 10 and 13). Secondly, circulations induced by the moving cloud cover gave subsidence at the rear edge of the anvil, leading to warmer, drier air at the aircraft altitude (Figure 2(d), and (Marsham *et al.*, 2007, Figure 16)). In addition, observations and LEM simulations show that the time lag in entrainment compared with surface fluxes stratified the boundary layer under the cirrus, and this stratification may have trapped warm, moist thermals in an internal layer, but this process did not contribute to the warmer, drier boundary layer observed under the cirrus cloud.

3.2. Pre-existing variations in boundary-layer moisture

The effects of cirrus shading on the boundary layer raise the question of whether the variations in cirrus shading could have led to the lack of drying in the boundary layer observed at Reading from 10:00 UTC, compared with the other radiosonde sites (Figure 2). Figure 15 shows results from LEM simulations initialized with the 9:00 UTC Chilbolton or Reading radiosonde profiles and forced

with surface fluxes calculated from Meteosat 11 μm BTs from Chilbolton or Reading (Marsham *et al.*, 2007). The clearest effect seen in Figure 15 is from the differences between the initially-weaker lid at Reading and the initially-stronger lid at Chilbolton. The thinner cirrus cover at Reading gives larger surface fluxes, which allow a deeper boundary layer to develop, but the boundary layer is drier than if the fluxes from Chilbolton are used. This suggests that the lack of drying observed at Reading was not related to the differences in cirrus cover.

Retrievals of column-integrated WVMR from Global-Positioning-System (GPS) data (Bevis *et al.*, 1992) show that at 9:00 UTC the atmosphere northeast of Chilbolton held more water vapour than that to the west of Chilbolton (Figure 16). At 9:00 UTC, 14% of the variance in the column-integrated WVMRs from radiosondes was due to differences above 800 m (approximately the top of the boundary layer). So although the GPS retrievals are of total-column water vapour, we expect the variability to be dominated by boundary-layer variations. The southwest-to-northeast gradient shown by the GPS retrievals is consistent with the radiosonde observations of a wetter boundary layer at Reading compared with the other radiosonde sites (Figure 2), the differences of around 1.5 kg m^{-2} between Reading and Bath corresponding to a difference of 1.9 g kg^{-1} over the boundary

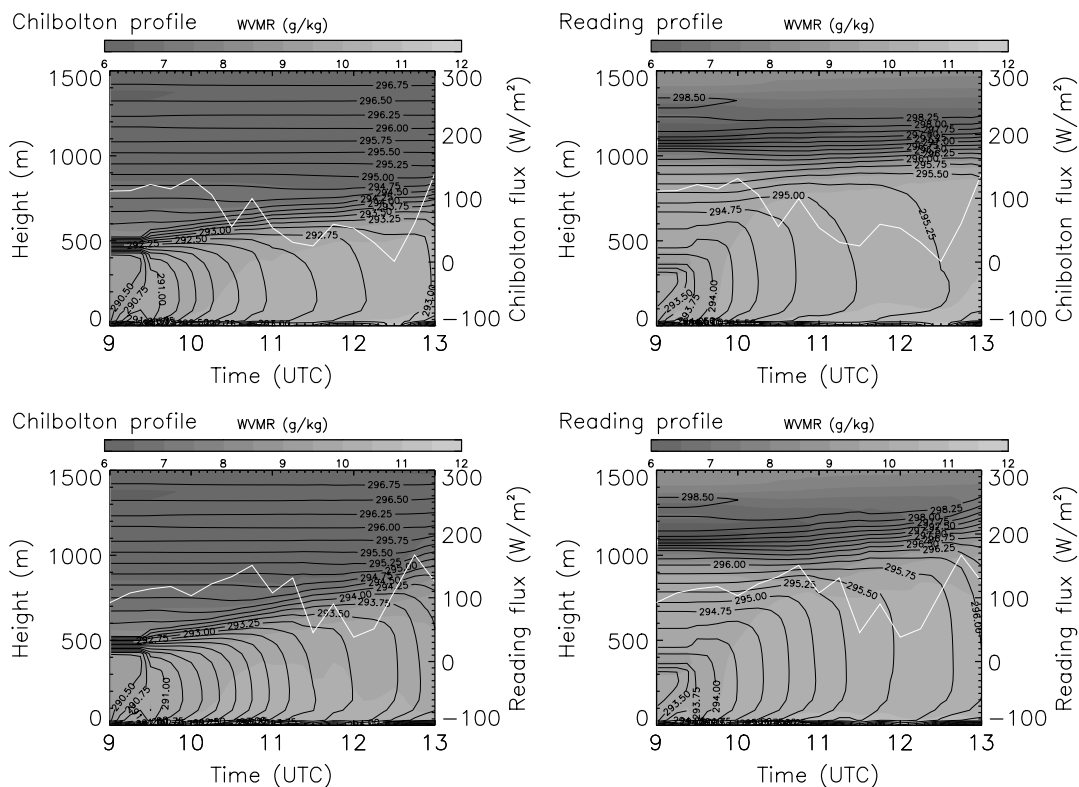


Figure 15. As Figure 14(a), but for simulations initialized with the 9:00 UTC Chilbolton profile (left) or the Reading 9:00 UTC profile (right), and forced with surface fluxes estimated from 11 μm Meteosat BTs from Chilbolton (top) or Reading (bottom).

layer compared with the 1.7 g kg^{-1} shown by radiosondes. This gradient in column-integrated WVMRs was present from 08:30 UTC (before the arrival of the cirrus anvils) until at least 14:00 UTC, and so was clearly not a result of the cirrus cover (we do not expect the variations induced by the cirrus shading to be detectable in the GPS retrievals, because of the limited data resolution and the vertical integration of the WVMRs). This spatial variation in boundary-layer moisture was perhaps due instead to a different Bowen ratio at Reading, or to the dissipating low-level stratiform cloud observed there (Figure 1).

4. Conclusions

Aircraft observations of the boundary layer from CSIP IOP 5 show that cirrus shading led to reduced WVMRs and increased potential temperatures at around 500 m in the boundary layer: at 500 m the boundary layer was 0.8 g kg^{-1} drier and 0.3 K warmer than under clear skies. In addition, there were fewer strong moist updraughts observed under the cirrus cover. These effects would have inhibited the development of convective clouds under the cirrus, and so are consistent with the conclusions of (Marshall *et al.*, 2007).

The occurrence of warmer, drier air under the cirrus is understood to have been caused by a combination of two mechanisms. First, the shading led to a less-developed boundary layer in shaded areas. Secondly, circulations induced by the moving cloud cover gave

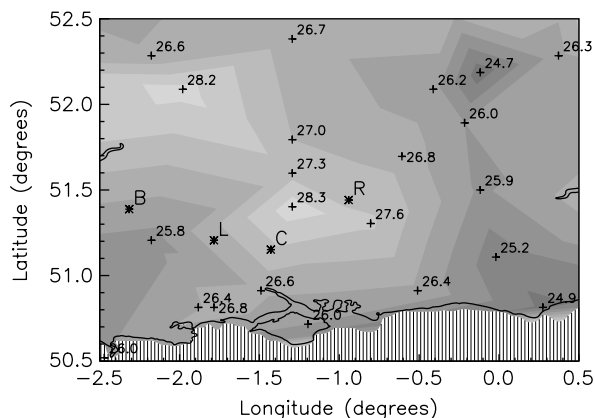


Figure 16. Column-integrated WVMRs retrieved from GPS data (kg m^{-2}) at 09:00 UTC. The locations of individual retrievals are shown by crosses, and these have been interpolated to give the grey-shaded field. This interpolation should be used as a guideline only, especially in data-sparse areas, and is not valid near the southern edge of the domain, because of the absence of observations over the sea. The locations of the Bath, Larkhill, Chilbolton and Reading radiosonde sites are shown by the letters 'B', 'L', 'C' and 'R', respectively.

subsidence at the rear edge of the anvil. LEM simulations show that the first effect is expected to lead to a warmer, drier boundary layer ahead of the cirrus and a colder, drier boundary layer behind (Figure 13). This is consistent with correlations between boundary-layer variables observed from aircraft and time-lagged Meteosat observations (Figure 10). We showed in the first part of

this study (Marsham *et al.*, 2007, Figure 16) that subsidence at the top of the boundary layer is expected to have been maximum at the rear edge of the cirrus anvils. This is consistent with radiosonde observations from Bath (Figure 2(d)), which had the lowest 11 μm BTs of all the radiosonde sites, and also with wind-profiler observations of boundary-layer depth (Figure 4). The subsidence is expected to have led to a warming of a magnitude consistent with the differences observed. This paper therefore provides (as far as the authors are aware) the first published observational evidence of mesoscale circulations induced by rapidly-moving (approximately 15 ms^{-1}) areas of cloud cover of limited spatial extent (approximately 50 km diameter), although this evidence is rather indirect. Marsham *et al.* (2007) suggested that these circulations were significant for convective initiation.

Cirrus shading reduced surface fluxes (Marsham *et al.*, 2007, Section 3), and effects on boundary-layer turbulence were observed using aircraft data and a 1290 MHz wind profiler. Both show that the turbulence minimum in the boundary layer lagged the surface flux minimum by 30–45 min. This is supported by high-resolution (50 m horizontal grid spacing) three-dimensional LEM simulations. This led to the persistence of entrainment at the top of the boundary layer after the onset of cirrus cover, which stabilized the previously well-mixed boundary layer (Figure 2(a) and (c) and Figure 14).

Aircraft observations of vertical velocities are dominated by variability on scales comparable to the boundary-layer depth, as expected. These scales can be seen in power spectra of potential temperature and WVMR, although for these variables mesoscale variations are comparable or dominant. Interestingly, a spectral gap is observed at around 6 km between the mesoscale and the boundary-layer-scale contributions to these power spectra in data from the aircraft that flew under both thick cirrus and clear skies, but not from the other aircraft, which flew only under moderate cirrus cover. It is possible that this moderate cirrus cover suppressed the boundary-layer convection, and the lack of cirrus variability reduced mesoscale variability, making this spectral gap less clear.

Variations in boundary-layer moisture that pre-dated the effects of the cirrus have been shown to be significant for convection in LEM simulations, as well as in terms of CAPE and CIN. These variations had a maximum magnitude similar to the variations induced by the cirrus cover (about 2 g kg^{-1}). The boundary layer at Reading was initially moister than at the other radiosonde sites, and this moist boundary layer was maintained, unlike at the other sites. This moister boundary layer at Reading is detectable in retrievals of column-integrated WVMR from GPS data. LEM simulations show that the lack of drying at Reading was not due to variations in cirrus shading, but perhaps due to spatial variations in the Bowen ratio, or the dissipating low stratiform cloud observed at Reading. In addition, the initially-weaker lid at Reading allowed much more rapid boundary-layer

growth at this site, showing the importance for NWP of capturing the initial spatial variability of this lid.

The fact that temperature and moisture variations were dominated by the mesoscale is perhaps encouraging for NWP, since these larger-scale variations can be resolved well by NWP models, unlike the variations on the scale of the boundary layer. The variations in boundary-layer WVMRs that pre-dated the arrival of the cirrus are detectable in retrievals of column-integrated WVMR from GPS data, highlighting the potential for assimilation of these data. However, this paper shows that much of this mesoscale variability was caused by shading from cirrus anvils. Representing these cirrus-shading effects is a challenge for forecasting and data assimilation, since NWP models do not resolve shallow internal layers well and it difficult to predict the details of the cirrus anvils produced by convective storms.

Acknowledgements

We would like to thank the Met Office for the Larkhill radiosonde data, and all those involved in the CSIP field campaigns, particularly the CSIP radiosonde teams and the crew of the Dornier 128 research aircraft of the Institute of Flight Guidance from the University of Braunschweig. Retrievals of column-integrated water vapour from GPS data were provided by Jonathan Jones (Met Office, UK), Etienne Orliac (Institute of Engineering Surveying and Space Geodesy, Nottingham University, UK) and Galina Dick and Markus Ramatschi (GeoForschungsZentrum, Potsdam, Germany). Comments from one anonymous reviewer resulted in significant improvements to this paper, and we would like to thank both reviewers for their valuable comments. This project was funded by the Natural Environment Research Council (NERC): NER/O/S/2002/00971.

References

- Bevis M, Businger S, Herring TA, Rocken C, Anthes RA, Ware RH. 1992. GPS meteorology – remote sensing of atmospheric water-vapor using the global positioning system. *J. Geophys. Res. – Atmos.* **97**: 15 787–15 801.
- Browning K, Blyth A, Clark P, Corsmeier U, Morcrette C, Agnew J, Bamber D, Barthlott C, Bennett L, Beswick K, Bitter M, Bozier K, Brooks B, Collier C, Cook C, Davies F, Deny B, Engelhardt M, Feuerle T, Forbes R, Gaffard C, Gray M, Hankers R, Hewison T, Huckle R, Kalthoff N, Khodayar S, Kohler M, Kraut S, Kunz M, Ladd D, Lenfant J, Marsham J, McGregor J, Nicol J, Norton E, Parker D, Perry F, Ramatschi M, Ricketts H, Roberts N, Russell A, Schulz H, Slack E, Vaughan G, Waight J, Watson R, Webb A, Wieser A, Zink K. 2006a. The Convective Storm Initiation Project. *Bull. Am. Meteorol. Soc.* (to appear).
- Browning K, Morcrette C, Blyth A, Bennett L, Clark P, Corsmeier U, Agnew J, Barkwith A, Barthlott C, Behrendt A, Bennett A, Beswick K, Bozier K, Brooks B, Chalmers N, Collier C, Cook C, Dacre H, Davies F, Davies L, Davies O, Deny B, Devine G, Dixon M, Engelhardt M, Fitch A, Forbes R, Gaffard C, Gallagher M, Goddard J, Gray M, Hewison T, Huckle R, Illingworth A, Kalthoff N, Keeley S, Khodayar S, Kilburn C, Kohler M, Kottmeier C, Kraut S, Ladd D, Lean H, Lenfant J, Marsham J, McGregor J, Mobbs S, Nicol J, Norton E, Parker D, Perry F, Ramatschi M, Richardson A, Ricketts H, Roberts N, Russell A, Slack E, Vaughan G, Watson R, Webb A, Weckwerth T, Wieser A, Wilson J, Wrench C, Wulfmeyer V, Zink

- K. 2006b. 'A summary of the Convective Storm Initiation Project Intensive Observation Periods'. Met Office Forecasting Research Technical Report: 474/JCMM Report 153.
- Couvreux F, Guichard F, Redelsperger JL, Kiemle C, Masson V, Lafore JP, Flamant C. 2005. Water-vapour variability within a convective boundary-layer assessed by large-eddy simulations and IHOP-2002 observations. *Q. J. R. Meteorol. Soc.* **131**(611): 2665–2693.
- Crook A. 1991. 'Small-scale moisture variability in the convective boundary layer and its implications for nowcasting'. Pp 67–70 in *25th Conf. on Radar Meteor. (9)*, Paris, France.
- Gray MEB, Petch J, Derbyshire SH, Brown AR, Lock AP, Swann HA. 2001. 'Version 2.3 of the Met. Office large eddy model'. Met Office (APR) Turbulence and Diffusion Rep. 276. Met Office, Exeter, UK.
- Jonker HJJ, Duynkerke PG, Cuijpers JWM. 1999. Mesoscale fluctuations in scalars generated by boundary layer convection. *J. Atmos. Sci.* **56**(5): 801–808.
- Mahrt L. 1991. Boundary-layer moisture regimes. *Q. J. R. Meteorol. Soc.* **117**(5): 151–176.
- Marsham JH, Morcrette CJ, Browning KA, Blyth AM, Parker DJ, Corsmeier U, Kalthoff N, Kohler M. 2007. Variable cirrus shading during CSIP IOP 5. I: Effects on the initiation of convection. *Q. J. R. Meteorol. Soc.* **133**: 1643–1660.
- Van der Hoven I. 1957. Power spectrum of horizontal wind speed in the frequency range from 0.0007 to 900 cycles per hour. *J. Meteorol.* **14**: 160–164.
- Weckwerth TM. 1999. The effect of small-scale moisture variability on thunderstorm initiation. *Mon. Weather Rev.* **128**(12): 4017–4030.
- Weckwerth TM, Wilson JW, Wakimoto RM. 1996. Thermodynamic variability within the convective boundary layer due to horizontal convective rolls. *Mon. Weather Rev.* **124**(5): 769–784.
- Wilson JW, Roberts RD. 2006. Summary of convective storm initiation and evolution during IHOP: Observational and modeling perspective. *Mon. Weather Rev.* **134**(1): 23–47.